



RESEARCH ARTICLE

# Digital generation of super-Gaussian perfect vortex beams via wavefront shaping with globally adaptive feedback

Rui Ma<sup>1,2,†</sup>, Ke Hai Luo<sup>1,†</sup>, Jing Song He<sup>2,5</sup>, Wei Li Zhang<sup>3</sup>, Dian Yuan Fan<sup>1</sup>, Anderson S. L. Gomes<sup>4</sup>, and Jun Liu<sup>1</sup>

<sup>1</sup>International Collaborative Laboratory of 2D Materials for Optoelectronics Science and Technology of Ministry of Education, Institute of Microscale Optoelectronics, Shenzhen University, Shenzhen, China

<sup>2</sup>Institute for Advanced Study, Shenzhen University, Shenzhen, China

<sup>3</sup>Fiber Optics Research Centre, School of Information and Communication Engineering, University of Electronic Science and Technology of China, Chengdu, China

<sup>4</sup>Departamento de Física, Universidade Federal de Pernambuco, Recife-PE, Brazil

<sup>5</sup>Email: [hejingsong@szu.edu.cn](mailto:hejingsong@szu.edu.cn)

(Received 5 October 2023; revised 17 November 2023; accepted 22 November 2023)

## Abstract

High-intensity vortex beams with tunable topological charges and low coherence are highly demanded in applications such as inertial confinement fusion (ICF) and optical communication. However, traditional optical vortices featuring nonuniform intensity distributions are dramatically restricted in application scenarios that require a high-intensity vortex beam owing to their ineffective amplification resulting from the intensity-dependent nonlinear effect. Here, a low-coherence perfect vortex beam (PVB) with a topological charge as high as 140 is realized based on the super-pixel wavefront-shaping technique. More importantly, a globally adaptive feedback algorithm (GAFA) is proposed to efficiently suppress the original intensity fluctuation and achieve a flat-top PVB with dramatically reduced beam speckle contrast. The GAFA-based flat-top PVB generation method can pave the way for high-intensity vortex beam generation, which is crucial for potential applications in ICF, laser processing, optical communication and optical trapping.

**Keywords:** digital micromirror device; flat-top beam; orbital angular momentum; perfect vortex beam; random fiber laser

## 1. Introduction

Vortices exist ubiquitously in different disciplines of physics, from fluid dynamics to optics. Vortex beams carrying orbital angular momentum (OAM) can greatly promote the development of light–matter interactions that have particular significance for fundamental physics and cutting-edge techniques<sup>[1–8]</sup>. Although paraxial eigen modes such as the Laguerre-Gaussian modes have a propagation invariant beam structure, the intrinsic OAM-dependent radial structure also greatly limits its application prospects in high-intensity related applications, such as inertial confinement fusion (ICF). Unlike OAM eigen modes, so-called perfect vortex beams (PVBs) feature a size-tunable and OAM-independent annulus profile, which can be used

for effective OAM mode multiplexing in the high-capacity communication system as well as in optical trapping<sup>[9,10]</sup>.

Generally, a high-intensity beam with uniform intensity distribution and low coherence is preferred in ICF to uniformly compress and heat the fuel target<sup>[11–13]</sup>. The further combination of a vortex beam could control the laser plasma, which would directly affect the fuel density and temperature that are crucial for fusion ignition<sup>[14,15]</sup>. In addition, the realization of the high-intensity beam also relies on uniform amplification by avoiding the intensity-dependent nonlinear effects<sup>[12,13]</sup>. However, conventional PVBs with nonuniform annulus intensity are not very suitable for relay signal amplification and firm particle trapping<sup>[16]</sup>. Although conventional flat-top beams have been investigated widely, they mainly concentrate on an intensity-only profile, not the vortex field that is preferred here. Therefore, all of these features pose a great demand for vortex beam shaping not only in the topological charge but also in the transverse intensity profiles. On the other hand, for temporal coherence, non-polarized vortex light from a random fiber laser (RFL)

Correspondence to: Jun Liu, International Collaborative Laboratory of 2D Materials for Optoelectronics Science and Technology of Ministry of Education, Institute of Microscale Optoelectronics, Shenzhen University, Shenzhen 518060, China. Email: [liuj1987@szu.edu.cn](mailto:liuj1987@szu.edu.cn)

<sup>†</sup>These authors contributed equally to this work.

can contribute to a low-coherence laser seed that is greatly desirable in ICF<sup>[17]</sup> but cannot be efficiently created by a conventional liquid-crystal-based spatial light modulator directly using the non-polarized RFL. Aiming at addressing these requirements, a high-quality laser seed, that is, a low-coherence PVB with both a flat-top intensity profile and a flexibly manipulated high topological charge, is urgently needed, which has been seldom investigated to date.

Here, we report a flexibly tunable low-coherence PVB generation based on the super-pixel wavefront-shaping technique by employing a polarization-independent digital micromirror device (DMD) and an RFL light source. The topological charge of the low-coherence PVB has been optimized to as high as 140. More importantly, to address the nonuniform intensity distribution, we propose a globally adaptive feedback algorithm (GAFA) to further optimize the super-Gaussian PVB, which can efficiently suppress the intensity fluctuation and produce a flat-top PVB with a tunable high topological charge. In the GAFA-based wavefront-shaping operation, the feedback of the target intensity is considered individually in combination with a weighting and average filtering process. Theoretical and experimental results coincide well for the PVB generation process, while it is worth noting that the theoretically calculated beam speckle contrast value is only achieved under the ideal speckle suppression condition, which is difficult to achieve in practice. The proposed flat-top PVB generation technique can not only alleviate the requirements for ideal incident illumination but also provide a route to achieving high-quality vortex beams for various important applications.

## 2. Results

### 2.1. Perfect vortex beam generation

Conventional vortex beams, or rather, the paraxial eigenmodes carrying OAM, such as the Laguerre-Gaussian modes, have a topological charge dependent ring radius, that is, the diameter of the central dark hollow increases gradually with the growth of the topological charge<sup>[18]</sup>. In contrast, PVBs are featured with size-tunable and OAM-independent annulus patterns despite only being true at the Fourier plane. This ‘perfect’ OAM-carrying light provides a unique interface of light-matter interaction and thus has important applications in optical trapping and manipulation, quantum information processing<sup>[19]</sup>, etc. The complex field of an ideal PVB with the topological charge of  $l$  is defined in the following model<sup>[9]</sup>:

$$E_l(r, \varphi) = \delta(r - r_0) \exp(il\varphi), \quad (1)$$

where  $(r, \varphi)$  denote the polar coordinates,  $\delta$  is the Dirac delta function and  $r_0$  defines the radius of the PVB. Theoretically,

the  $\delta$  function can be approximated by using the Bessel series. However, the Bessel series expansion still depends on the topological charge value, which goes against the original intention of PVB generation. Besides, the intensity profile generated by the Bessel series expansion is also accompanied by the inevitable side lobes, which can degrade the vortex mode purity. Therefore, a Gaussian apodization method is employed here as defined in the following model<sup>[20,21]</sup>:

$$E_l(r, \varphi) = \exp(-(r - r_0)^2 / \Delta r^2) \exp(il\varphi), \quad (2)$$

where  $r_0$  and  $\Delta r$  represent the radius and width of the Gaussian-shaped annulus, respectively. The intensity profile is completely independent of the value of the topological charge, while the radius and width of the PVB can be flexibly tailored.

Figure 1 depicts a schematic diagram of the PVB generation and the corresponding characterization (see Section 4 for details). The experimental setup consists of three major parts: an incident light source, a vortex beam generation section using the super-pixel wavefront-shaping technique and a Mach-Zehnder interferometer for the vortex phase verification.

To facilitate the potential use in the ICF application mentioned above, we chose the well-known RFL as the incident light to be converted<sup>[22]</sup>. The RFLs have been extensively studied and widely applied in applications such as high-power<sup>[23,24]</sup> and high-efficiency lasing<sup>[25]</sup>, flexibly tunable<sup>[26–28]</sup> and special wavelength emission<sup>[29,30]</sup>, supercontinuum generation<sup>[31]</sup> and narrow linewidth lasing<sup>[32]</sup>. In particular, the low-coherence feature of RFLs makes them easy to be scaled up to high-intensity beams. Recently, a spectrum-tailored low-coherence RFL has been amplified to megawatt-class peak power, which shows great potential for the ICF laser facility<sup>[17]</sup>. The salient properties of RFLs are highlighted by the non-resonant lasing structure, the strongly suppressed temporal intensity fluctuation<sup>[33]</sup> and the low spatial coherence<sup>[34]</sup>, which are promising for the laser seed of ICF. Although random vortex beams have been reported based on the spatial light modulator<sup>[35]</sup> and long period fiber grating<sup>[36]</sup>, the performances in terms of the achievable topological charge and the beam profile quality still have huge room for improvement. Here, a half-open cavity-based random lasing light source is employed. The optical feedback is provided by a highly reflective fiber Bragg grating (HR-FBG) point reflector and the random distributed backscattered Rayleigh scattering along a single-mode fiber (SMF), while the optical amplification is provided by the active gain of a ytterbium-doped fiber (YDF). The characteristics of the employed low-coherence random lasing light source are discussed in detail in [Supplementary Note 1](#). More importantly, both the lasing spectrum and the maximum output power

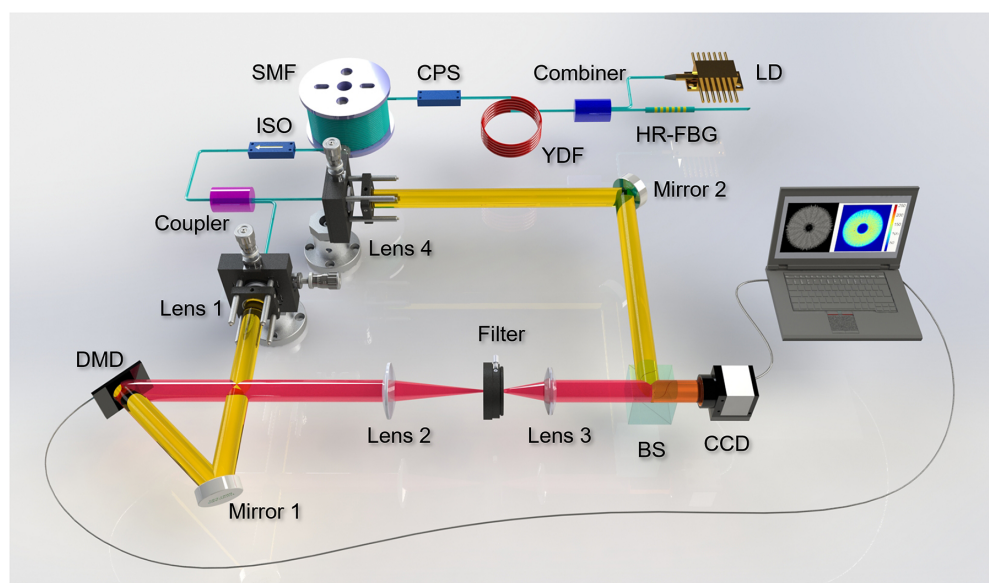


**Figure 1.** Schematic diagram of the PVB generation and the corresponding characterization sections. LD, laser diode; HR-FBG, high-reflectivity fiber Bragg grating; YDF, ytterbium-doped fiber; CPS, cladding power stripper; SMF, single-mode fiber; ISO, isolator; DMD, digital micromirror device; BS, beam splitter; CCD, charge-coupled device.

of the random lasing can be flexibly modulated, which facilitates the vortex beam generation and its potential application in ICF. It is worth noting that a polarized RFL can also be excited by replacing the polarization-independent fiber and components with polarization-dependent ones.

Typically, the generation of vortex beams can be classified into passive and active. For passive generation, a Gaussian beam can be converted into a vortex beam by employing a spiral phase plate<sup>[37]</sup> q-plate<sup>[38]</sup>, long period fiber grating<sup>[39]</sup> or spatial light modulator<sup>[40]</sup>, while for the latter approach, the vortex laser emission is directly excited within a resonant cavity<sup>[41,42]</sup>. Here, super-pixel wavefront shaping, which only employs a binarized spatial light modulator<sup>[43]</sup>, that is, a DMD, is applied to excite the PVB. The DMD-based light field modulation has significant advantages due to its high-speed light modulation, relatively broadband spectral response, polarization-independent incident light and excellent power handling capability. Therefore, DMD-based structure light modulation is particularly suitable for incoherent incident light. Recently, super-pixel wavefront shaping has also been widely used for vortex beam generation<sup>[21,44–46]</sup>. In the super-pixel wavefront-shaping technique, contiguous pixels (e.g.,  $4 \times 4$  pixels) on the DMD plane compose a so-called super-pixel that links with one pixel on the output imaging plane. By selectively turning on the individual DMD pixels, versatile light modulation in the complex field (i.e., both the amplitude and the phase profiles) can be realized with a spatial filter deployed on the Fourier plane of a  $4f$  system that segregates the first-order diffraction light from the others. A binarized DMD pattern could be transformed from the target intensity and

phase profiles through a pre-calculated lookup table, which is further loaded on the DMD and shapes the incident beam.

For external modulator-based passive vortex beam generation, another key factor that determines the quality of the vortex beam is the performance of the employed modulator, for example, the total number of modulation elements and the size of each element. Vortex beam generation with a super-high topological charge, that is, a more delicate and complex phase variation in the azimuthal direction, places a much higher demand on the number of involved modulation elements. To make full use of the DMD pixels and achieve a topological charge as high as possible with the super-pixel wavefront-shaping technique, the radius of the vortex beam is supposed to be enlarged while decreasing its width. Therefore, two typical groups of PVB (i.e., one group with lower topological charges and the other with higher topological charges) generation have been considered here as representatives, as shown in Figure 2. Here, for the lower topological charge group ( $l = 1, 2$  and  $3$ ), the radius  $r_0$  and width  $\Delta r$  of the annulus are 1.88 and 0.869 mm, respectively, while for the higher topological charge group ( $l = 50, 100$  and  $140$ ), these values are 3.91 and 0.290 mm. The target PVB intensity profiles are shown in Figure 2(a). Figure 2(b) gives the corresponding phase profiles relative to Figure 2(a). It is clear that for the high topological charge group, the phase front in the central region is distorted dramatically, which is limited by the mesh grid precision. However, the phase front still fulfills the periodicity determined by the topological charge in the outer region that is overlapped with the target intensity. Using the target intensity and phase profiles, the binary DMD patterns can be produced in the super-pixel wavefront shaping, as displayed in Figure 2(c).

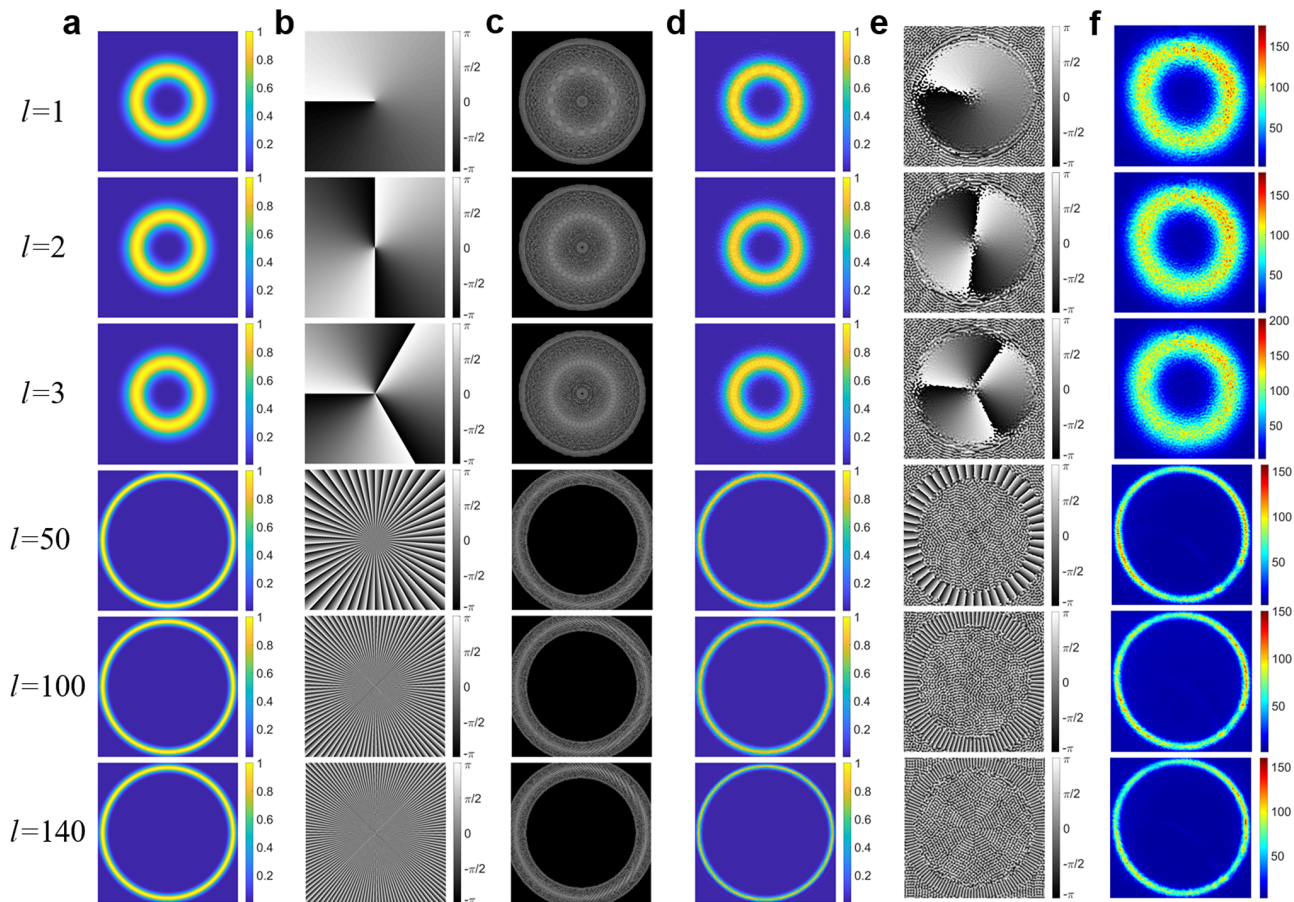


**Figure 2.** Generation of a PVB using super-pixel wavefront shaping. The target intensity (a) and phase (b) profiles of the PVBs. (c) Binary DMD patterns. Theoretical intensity (d) and phase (e) profiles of the output using super-pixel wavefront shaping. (f) Experimentally measured intensity profiles.

With the generated DMD patterns, the desired PVB output is the first-order diffraction light in a  $4f$  system, which should be filtered out from the outgoing mode of the DMD by placing an iris diaphragm on the Fourier plane. This process could be numerically calculated based on wave optics:

$$E_o = \text{FT}^{-1} \{ \text{FT} \{ D \} \cdot M \}, \quad (3)$$

where  $\text{FT}$  and  $\text{FT}^{-1}$  denote the Fourier transform and inverse Fourier transform, respectively,  $E_o$  is the output optical field,  $D$  is the binary DMD pattern and  $M$  is a circular aperture-based Fourier mask. In this sense, the PVB generation scheme using an individual DMD pattern could be verified in advance by the fidelity of the calculated intensity and phase profiles, as shown in Figures 2(d) and 2(e), respectively. Both the intensity and phase profiles generated by the binary DMD patterns in Figure 2(c) are in excellent agreement with the original targets in Figures 2(a) and 2(b). Finally, the binary DMD patterns are loaded on the DMD and the experimentally measured intensity profiles are given in Figure 2(f). The obtained PVBs are also in accordance with the calculated intensity profiles, while for each PVB group,

the radius and the width of the intensity profile remain the same regardless of the topological charge.

Apart from the topological charge-independent intensity profiles, the characteristics of the generated PVBs are also further investigated in [Supplementary Note 2](#). Firstly, the helical phase front of the generated PVBs is verified by employing the Mach-Zehnder interferometer, even for the highest topological charge front. To obtain a high-intensity PVB, subsequent amplification stages are essential. Generally, the gain profile in the amplifier is spatially uniform, and the incident laser beam possessing a good spatial uniformity is crucial to boosting its intensity<sup>[12]</sup>. Therefore, the flatness of the obtained PVBs is also detailedly investigated. Here, speckle contrast  $C$  defined by  $\sigma_I / \langle I \rangle$  (where  $\sigma_I$  denotes the standard deviation of the intensity and  $\langle I \rangle$  is the average intensity) is employed to quantitatively evaluate the flatness of the PVBs. All the central cross-section curves of the PVBs and the beam speckle contrasts verify that the conventional Gaussian model-based PVBs are far from a typical flat-top beam, which means that Gaussian model-defined PVB generation is not suitable to realize a high-quality flat-top PVB.

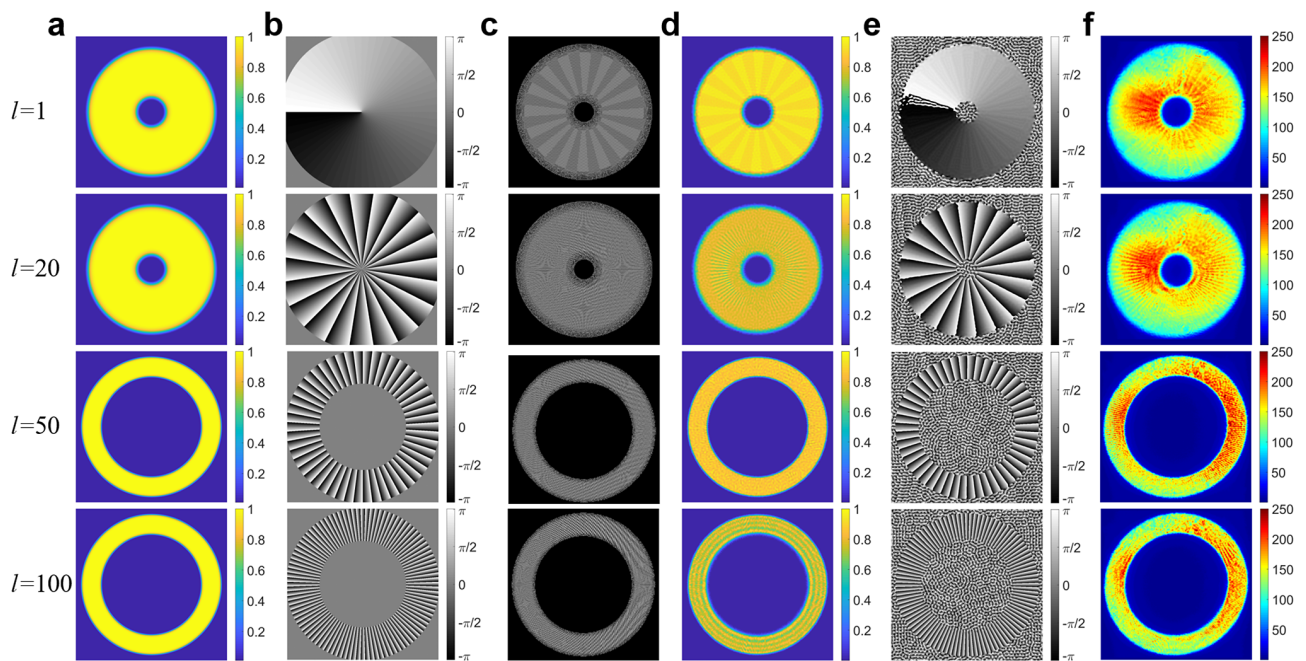


**Figure 3.** Flat-top PVB generation. The target intensity (a) and phase (b) profiles of the flat-top PVBs. (c) Binary DMD patterns. Theoretical intensity (d) and phase (e) profiles of the flat-top PVBs. (f) Experimentally measured intensity profiles.

## 2.2. Flat-top perfect vortex beam generation

It is noticed that the conventional Gaussian model-defined target intensity should be further optimized when trying to excite a flat-top PVB. To address this problem, a super-Gaussian apodization is employed for the flat-top PVB generation as defined in the following equations<sup>[47]</sup>:

$$E_l(r, \varphi) = C_\alpha \exp(-(r - r_0)^\alpha / \Delta r^\alpha) \exp(il\varphi), \quad (4)$$

$$C_\alpha = 2^{1/\alpha} / \sqrt{\pi \Delta r^2 \Gamma((\alpha + 2) / \alpha)}, \quad (5)$$

where  $\alpha = 2, 3, 4, \dots$  is the order of the super-Gaussian mode. By increasing the value of  $\alpha$ , the flatness of the beam improves dramatically with gradually decreased inner and outer edges. Here, the super-Gaussian order  $\alpha$  is set to 14, and the corresponding target intensity and phase profiles are given in Figures 3(a) and 3(b). Compared with a directly binarized annulus target intensity that has suddenly changed edges, the smooth feature of the inner and outer edges for the super-Gaussian apodization method guarantees that the spatial frequencies can be well transferred through the  $4f$  imaging system, which is conducive for flat-top beam generation. It is worth noting that to underline the role of the flat-top structure, the width of the target annulus should not be too narrow, especially for a PVB with super-high topological charge. Therefore, the widths of the target intensity in Figure 3(a) are 1.42 mm ( $l = 1, 20$ ) and 0.579 mm ( $l = 50, 100$ ), while the radii are 2.17 mm ( $l = 1, 20$ ) and 3.33 mm

( $l = 50, 100$ ). With the optimized flat-top target intensity (Figure 3(a)) and the target phase (Figure 3(b)) profiles, the binary DMD patterns are produced as given in Figure 3(c). In the same way, the theoretical intensity and phase profiles are calculated and illustrated in Figures 3(d) and 3(e), respectively. It is observed that the intensity profiles retain the major flat-top feature, even with some observable fluctuations. The beam speckle contrasts of the theoretical flat-top PVBs are also calculated to be 0.0208, 0.0535, 0.0371 and 0.0873 for  $l = 1, 20, 50$  and  $100$ , respectively. Therefore, the super-Gaussian apodization-based flat-top PVBs' target can theoretically suppress the intensity fluctuation in comparison with the conventional Gaussian model-based ones. However, the experimentally measured PVB intensity profiles shown in Figure 3(f) exhibit a quite different performance compared with the flat-top target. The inner annulus region has a much stronger intensity than the outer region, especially for the lower topological charge group, which means the simply imposed flat-top intensity target only mitigates the drawback to some extent and is incapable of realizing a qualified flat-top intensity in an experimental scenario.

In super-pixel wavefront shaping, the unmodulated incident beam is supposed to be an ideal plane wave that is uniformly distributed. However, in the practical experiment, the non-flat-top PVB can result in nonuniform incident illumination, that is, a Gaussian-shaped intensity distribution from a fiber laser. The degeneration of the intensity modulation in the super-pixel wavefront shaping due to the nonuniform illumination is discussed in detail in Supplementary Note 3. This means that under nonuniform incident illumination,

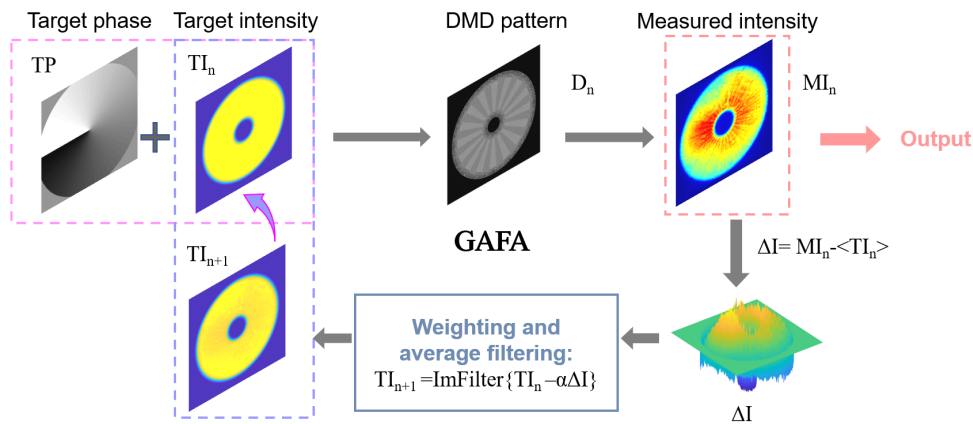


**Figure 4.** Block diagram of the GAFA-based wavefront shaping for flat-top PVB generation. TP, target phase; TI, target intensity; MI, measured intensity.

the ultimate modulated output is not simply determined by the target intensity, but also strongly depends on the characteristics of the incident light, for example, the intensity profile. Therefore, the ideal relations in Equation (3) should be optimized:

$$E_o = \text{FT}^{-1} \{ \text{FT} \{ D \cdot W_{\text{inc}} \} \cdot M \}, \quad (6)$$

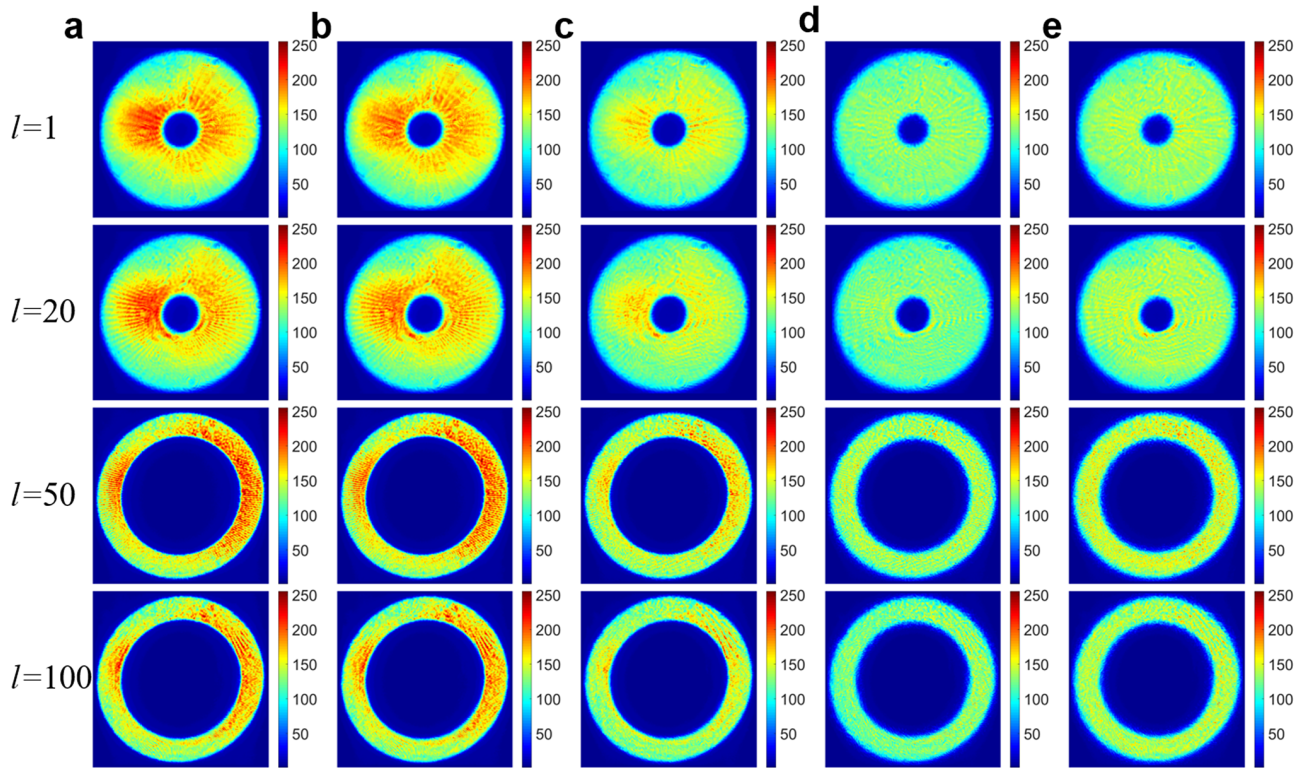
where  $W_{\text{inc}}$  is a weight factor determined by the incident intensity profile. It is naturally anticipated that the uniformity of the output light field can be optimized significantly by regulating the target intensity and the corresponding DMD pattern.

To suppress the nonuniform intensity distribution of the generated PVBs, GAFA-based wavefront shaping is proposed as the block diagram shown in Figure 4. For the  $n$ th iteration, using the target phase (TP) and target intensity ( $\text{TI}_n$ ), a binary DMD pattern  $D_n$  can be generated. After loading the  $D_n$  to the DMD, the measured intensity  $\text{MI}_n$  is captured on the camera. To regulate the target intensity, the difference between  $\text{MI}_n$  and  $\text{TI}_n$  is calculated by equation  $\Delta I = \text{MI}_n - \langle \text{TI}_n \rangle$  where ' $\langle \rangle$ ' denotes the averaging operation. The mean intensity value  $\langle \text{TI}_n \rangle$  then acts as a threshold to identify values larger or smaller in the real-time  $\text{MI}_n$ . It is worth noting that  $\Delta I$  is mainly used as a dimensionless parameter for characterization. Therefore, in the  $\Delta I$  profile, the non-negative values all correspond to the measured intensity, which is larger than the threshold and should be suppressed in the next iteration, while the negative values are smaller than the threshold and should be boosted. An updated target is obtained by taking the relation  $\text{TI}_n - \alpha \Delta I$ , where  $\alpha$  is a weighting factor to control the speed of feedback. To further smooth the intensity fluctuation and ameliorate the impact of the abnormal point, which is extremely larger or smaller than its surroundings, a 2D averaging filter is imposed on the generated  $\text{TI}_n - \alpha \Delta I$ , that is,  $\text{ImFilter}\{\text{TI}_n - \alpha \Delta I\}$ , which leads to the final updated target intensity pattern  $\text{TI}_{n+1}$ . The  $\text{TI}_{n+1}$  as well as the unchanged TP pattern is fed into the  $(n+1)$ th iteration.

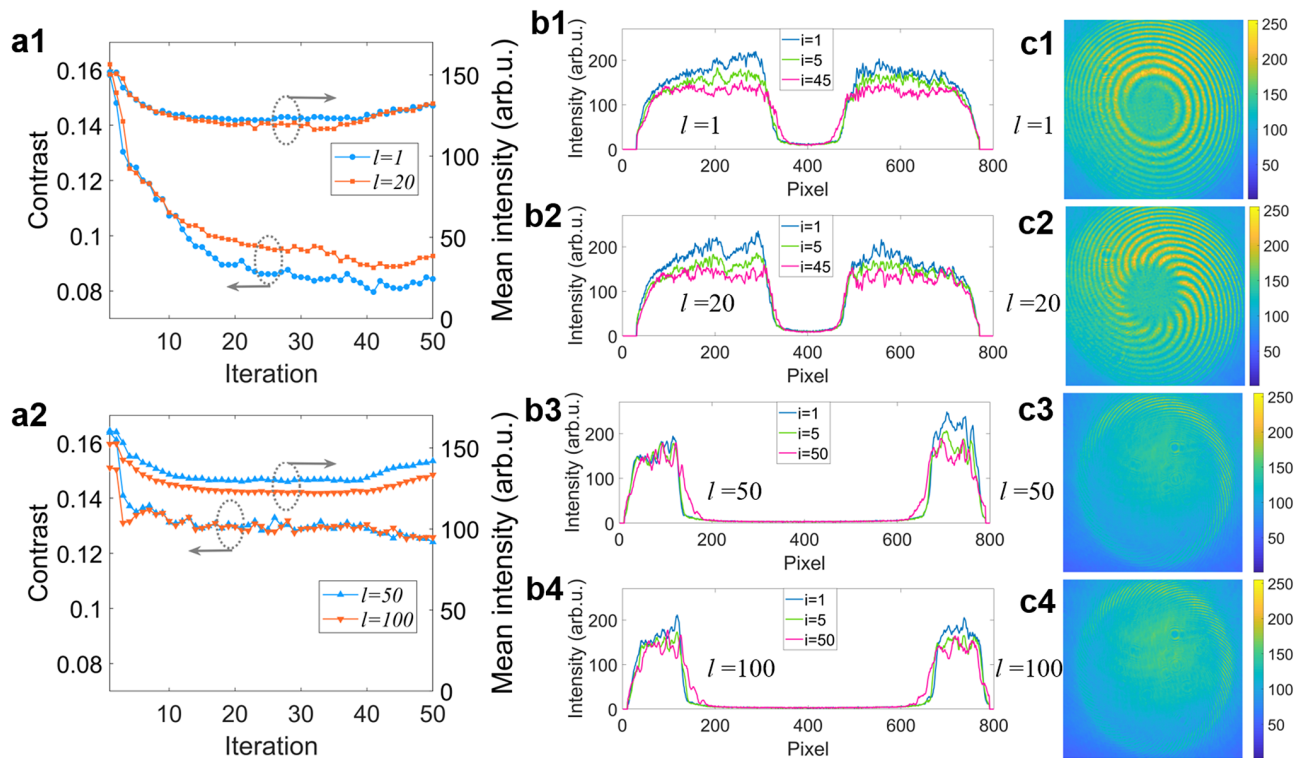
Therefore, adaptive modulation is only imposed on the target intensity in each iteration, while the target phase remains unaffected. Apparently, for each pixel to be modulated, it is not simply determined by the corresponding pixel from the last iteration, but also by all its surrounding pixels. Therefore, this global feedback for all of the involved modulation elements can greatly improve the efficiency to realize a flat-top PVB in practice.

Figure 5 shows the result of the GAFA-based wavefront shaping in realizing a flat-top PVB. Here, the parameters of the original target intensity and phase profiles are the same as those in Figure 3. With the increase of the feedback iteration number, the original intensity profiles in Figure 5(a) gradually become flat with strong suppression of the intensity in the inner annulus region. When the iteration number reaches 40, the intensity profiles in all four PVB cases exhibit excellent intensity uniformity, as shown in Figure 5(d). With another 10 iterations, the mean intensity of the PVB even increases. In addition, during the GAFA wavefront shaping, all the features of the annulus, that is, the radius, the width and the sharpness of the edge, remain unaffected, which indicates the robustness of the proposed method. Given that the frame rate of the employed DMD is 12.5 kHz, the optimization speed is restricted by the frame rate of the charge-coupled device (CCD) camera (i.e., 15 frames per second), which can be improved by using a high-speed CCD.

In order to give a more detailed analysis, the evolutionary characteristics of flat-top PVB generation using GAFA-based wavefront shaping are provided in Figure 6. Firstly, the beam speckle contrast and the mean intensity variation versus the iteration number are depicted in Figure 6(a). It is shown that for the lower topological charge group, the contrast is greatly reduced from the original 0.1582 to 0.0809 for  $l = 1$  and from 0.1620 to 0.0884 for  $l = 20$ , while for the higher topological charge group, the contrast is reduced from the original 0.1638 to 0.1241 for  $l = 50$  and from 0.1511 to 0.1253 for  $l = 100$ . It is observed that the contrast reduction is more notable for the group with a wider annulus (i.e., the lower topological charge groups  $l = 1$  and 20) compared to



**Figure 5.** Evolution of the measured intensity profiles under GAFA-based feedback modulation. (a) The unmodulated intensity profiles. (b)–(e) The real-time intensity profiles for iteration numbers 2, 5, 40 and 50, respectively.



**Figure 6.** Characteristics of flat-top PVB generation. Evolution of the speckle contrast and the mean intensity value for topological charges of 1 and 20 (a1), 50 and 100 (a2). Evolution of the curve in the central cross-section for the topological charges of 1 (b1), 20 (b2), 50 (b3) and 100 (b4). Interference patterns of the modulated flat-top PVB for the topological charges of 1 (c1), 20 (c2), 50 (c3) and 100 (c4).

those with a narrower annulus (i.e., the higher topological charge groups  $l = 50$  and  $100$ ). It is speculated that by involving a larger number of modulation elements and reducing the size of an individual element simultaneously, the residual intensity fluctuation could be further flattened and the beam speckle contrast could approach the theoretical values of the flat-top PVB calculated in Figure 3 as much as possible. In addition, the original Gaussian-shaped illumination profile also plays a great role in the deviation of the beam speckle contrast from theoretical ones since the Gaussian profile is far different from an ideal plane wave. Moreover, the mean intensity still maintains at a reasonable level without sacrificing too much, which indicates the high efficiency of the proposed GAFA-based wavefront shaping.

Secondly, the evolution of the curves in the central cross-section for the original beams and the beams after several feedback iterations is also given in Figure 6(b). The intensity in the inner region is strongly suppressed under the feedback modulation while the intensity in the outer region remains relatively stable. It can be interpreted that the proposed GAFA-based wavefront shaping is more powerful in suppressing the stronger intensity rather than boosting the lower intensity, which is limited by insufficient light illumination. This also accounts for the drop of the mean intensity for the first 20 iterations in Figure 6(a) due to the strongly suppressed inner intensities. After the inner and the outer intensities of the annulus become the same level, the mean intensity then gradually increases due to the speckle suppression and intensity redistribution with further adaptive modulation. Finally, the modulated flat-top PVBs are also verified through the Mach–Zehnder interferometer, as shown in Figure 6(c). The number of the spiral stripes extending outward from the center all coincides with the corresponding topological charge, which indicates that the proposed feedback modulation maintains the spiral phase feature. Therefore, with the assistance of the GAFA-based wavefront shaping, the original ununiform PVBs have all been modified into flat-top ones.

### 3. Discussion and conclusion

Low-coherence light sources have particular importance in applications such as ICF. As a spatial light modulator, DMD-based super-pixel wavefront shaping is preferred in regulating the non-polarized low-coherence RFL in contrast to a conventional liquid-crystal-based spatial light modulator that requires polarized incidence. By optimizing the annulus structure of the target PVBs, the achieved maximum topological charge here is 140. One needs to either upgrade the performance of the DMD (e.g., the amount of DMD pixels) or employ a more advanced wavefront-shaping algorithm to further increase the topological charge. On the other hand, even if the low-coherence light and the super-Gaussian apodization are combined, the experimentally

measured PVBs still show nonuniform intensity distribution, which is adverse to the realization of high-intensity PVBs. This is mainly attributed to the non-ideal illumination, that is, the plane wave. The proposed GAFA-based wavefront shaping can greatly suppress the laser speckle contrast. However, even though the experimentally realized contrasts are comparable to the conventional flat-top beams employed in high-intensity beam generation and ICF, there is still room for improvement according to the numerically calculated values. This could also be optimized by upgrading the performance of the DMD.

The realized flat-top PVB has great potential in practical applications. Firstly, for ICF and laser processing, the flat-top PVB can be directly used as the seed laser for high-intensity vortex beam generation by subsequent amplification stages. Secondly, in optical communications, the flat-top intensity profile benefits the expansion of the effective communication channel thanks to the alleviated intensity-dependent non-linear effect. Thirdly, the flat-top PVB can also provide a strong gradient force in the small inner annulus edge while maintaining a high topological charge, which can be used for the firm trapping application. In addition, it is speculated that the GAFA-based wavefront shaping could not only alleviate the requirements for uniform incident illumination in the generation of flat-top vortex beams but also efficiently increase the fidelity of the measured profile with respect to the target one.

In conclusion, low-coherence PVBs with high topological charges have been demonstrated by random fiber lasing and DMD-based super-pixel wavefront shaping. To address the nonuniform intensity distribution of the experimentally obtained low-coherence PVBs, the GAFA-based wavefront shaping is proposed, and flat-top PVBs with dramatically suppressed beam speckle contrast have been realized. The theoretical calculation of the beam generation coincides well with the experimental results, in terms of the variation tendency. It should be noted that the discrepancy between the theoretical speckle contrast and the experimental one results from the imperfect speckle suppression condition for the proposed method. It is speculated that GAFA-based wavefront shaping could not only alleviate the requirements for uniform incident illumination in the generation of flat-top vortex beams but also efficiently increase the fidelity of the measured profile with respect to the target one. More importantly, high-quality flat-top PVBs would facilitate potential applications that require high-intensity vortex beams, such as ICF, optical communication and optical trapping.

### 4. Experimental details

The fiber laser source employs a half-open cavity-based low-coherence random lasing structure that is composed of a 1064 nm HR-FBG (3 dB bandwidth, 2.6 nm), 5-m length YDF (Nufern, LMA-YDF-10/130-VIII) and a spool of 4-km

length SMF (YOFC, SM28). The cladding pump of the gain fiber is applied by injecting a 976 nm laser diode (LD) into the YDF through a signal/pump combiner. A cladding power stripper (CPS) is inserted between the YDF and the SMF to strip the unabsorbed pump light. To eliminate any potential feedback from the following parts and insure a half-open structure, an isolator (ISO) is fusion spliced at the distal end of the SMF.

To excite the vortex beam and characterize its phase profile, the output of the random lasing is split into two paths using a 3 dB coupler. Both of the output ports are mounted on a 2D translation stage and further collimated by a convex lens (focal length of 6.2 mm). For the vortex beam excitation path, the collected light irradiates on the surface of a DMD (1280×800 pixels, DLP650LNIR, Texas Instruments) via a highly reflective mirror. After being modulated by the loaded DMD pattern, the desired beam profile is filtered out in a 4f system (composed of two convex mirrors with focal lengths of 75 and 35 mm, respectively) where an iris diaphragm is placed on the Fourier plane to block all but the first-order diffraction light.

A Mach–Zehnder interferometer is built to characterize the spiral phase front of the generated vortex beam by introducing a reference beam and combining it with a vortex beam using a non-polarizing cube beam splitter (BS). Both the excited vortex beam profile and the interference pattern are monitored by a CCD (DCU224M, Thorlabs).

## Acknowledgements

This work was supported by the Guangdong Basic and Applied Basic Research Foundation (Grant No. 2020A151511143), the Natural Science Foundation of Guangdong Province (Grant Nos. 2021A1515011532 and 2023ZDZX3022) and Shenzhen Government's Plan of Science and Technology (Grant Nos. JCYJ20220818100019040, RCYX20210609103157071, and JCYJ20230808105713028).

## Supplementary Material

The supplementary material provides additional details on the characteristics of the random lasing light source (Note 1), characteristics of the generated PVBs (Note 2), and degeneration of the intensity modulation due to nonuniform illumination (Note 3). To view supplementary material for this article, please visit <http://doi.org/10.1017/hpl.2023.91>.

## References

1. L. Allen, M. W. Beijersbergen, R. J. C. Spreeuw, and J. P. Woerdman, *Phys. Rev. A* **45**, 8185 (1992).
2. J. Wang, J. Yang, I. M. Fazal, N. Ahmed, Y. Yan, H. Huang, Y. Ren, Y. Yue, S. Dolinar, M. Tur, and A. E. Willner, *Nat. Photonics* **6**, 488 (2012).
3. L. Paterson, M. P. MacDonald, J. Arlt, W. Sibbett, P. E. Bryant, and K. Dholakia, *Science* **292**, 912 (2001).
4. F. Tamburini, G. Anzolin, G. Umbricco, A. Bianchini, and C. Barbieri, *Phys. Rev. Lett.* **97**, 163903 (2006).
5. X. Fang, H. Ren, and M. Gu, *Nat. Photon.* **14**, 102 (2020).
6. R. Fickler, R. Lapkiewicz, W. N. Plick, M. Krenn, C. Schaeff, S. Ramelow, and A. Zeilinger, *Science* **388**, 640 (2012).
7. R. Fickler, G. Campbell, B. Buchler, P. K. Lam, and A. Zeilinger, *Proc. Natl. Acad. Sci. USA* **113**, 13642 (2016).
8. W. T. Buono and A. Forbes, *Opto-Electron. Adv.* **5**, 210174 (2022).
9. A. S. Ostrovsky, C. Rickenstorff-Parrao, and V. Arrizón, *Opt. Lett.* **38**, 534 (2013).
10. P. Vaity and L. Rusch, *Opt. Lett.* **40**, 597 (2015).
11. C. Labaune, *Nat. Phys.* **3**, 680 (2007).
12. Y. Cui, Y. Gao, D. Rao, D. Liu, F. Li, L. Ji, H. Shi, J. Liu, X. Zhao, W. Feng, L. Xia, J. Liu, X. Li, T. Wang, W. Ma, and Z. Sui, *Opt. Lett.* **44**, 2859 (2019).
13. Y. Gao, L. Ji, X. Zhao, Y. Cui, D. Rao, W. Feng, L. Xia, D. Liu, T. Wang, H. Shi, F. Li, J. Liu, P. Du, X. Li, J. Liu, T. Zhang, C. Shan, Y. Hua, W. Ma, Z. Sui, J. Zhu, W. Pei, S. Fu, X. Sun, and X. Chen, *Opt. Lett.* **45**, 6839 (2020).
14. J. Vieira and J. T. Mendonça, *Phys. Rev. Lett.* **112**, 215001 (2014).
15. W. Wang, K. Feng, L. Ke, C. Yu, Y. Xu, R. Qi, Y. Chen, Z. Qin, Z. Zhang, M. Fang, J. Liu, K. Jiang, H. Wang, C. Wang, X. Yang, F. Wu, Y. Leng, J. Liu, R. Li, and Z. Xu, *Nature* **595**, 516 (2021).
16. Y. Yang, Y. Ren, M. Chen, Y. Arita, and C. Rosales-Guzmán, *Adv. Photonics* **3**, 034001 (2021).
17. M. Fan, S. Lin, K. Yao, Y. Qi, J. Zhang, J. Zheng, P. Wang, L. Ni, X. Bao, D. Zhou, B. Zhang, K. Xiao, H. Xia, R. Zhang, P. Li, W. Zheng, and Z. Wang, *Matter Radiat. Extremes* **8**, 025902 (2023).
18. Y. Shen, X. Wang, Z. Xie, C. Min, X. Fu, Q. Liu, M. Gong, and X. Yuan, *Light Sci. Appl.* **8**, 90 (2019).
19. L. Zeng, Y. H. Ye, M. X. Dong, W. H. Zhang, E. Z. Li, D. C. Li, D. S. Ding, and B. S. Shi, *Opt. Lett.* **48**, 477 (2023).
20. M. Chen, M. Mazilu, Y. Arita, E. M. Wright, and K. Dholakia, *Opt. Lett.* **38**, 4919 (2013).
21. Y. Chen, Z. X. Fang, Y. X. Ren, L. Gong, and R. D. Lu, *Appl. Opt.* **54**, 8030 (2015).
22. S. K. Turitsyn, S. A. Babin, A. E. El-Taher, P. Harper, D. V. Churkin, S. I. Kablukov, J. D. Ania-Castañón, V. Karalekas, and E. V. Podivilov, *Nat. Photonics* **4**, 231 (2010).
23. Z. Wang, H. Wu, M. Fan, L. Zhang, Y. Rao, W. Zhang, and X. Jia, *IEEE J. Sel. Top. Quantum Electron.* **21**, 0900506 (2015).
24. H. Zhang, L. Huang, J. Song, H. Wu, P. Zhou, X. Wang, J. Wu, J. Xu, Z. Wang, X. Xu, and Y. Rao, *Opt. Lett.* **44**, 2613 (2019).
25. I. D. Vatnik, D. V. Churkin, E. V. Podivilov, and S. A. Babin, *Laser Phys. Lett.* **11**, 075101 (2014).
26. S. A. Babin, A. E. El-Taher, P. Harper, E. V. Podivilov, and S. K. Turitsyn, *Phys. Rev. A* **84**, 021805 (2011).
27. L. Zhang, H. Jiang, X. Yang, W. Pan, S. Cui, and Y. Feng, *Sci. Rep.* **7**, 42611 (2017).
28. Y. L. Zhang, S. S. Wang, M. Z. She, Y. J. Rao, and W. L. Zhang, *Photon. Res.* **11**, 20 (2023).
29. R. Ma, X. Quan, J. Liu, T. Zhao, and D. Y. Fan, *J. Lightwave Technol.* **40**, 3942 (2022).
30. H. Wu, W. Wang, Y. Li, C. Li, J. Yao, Z. Wang, and H. Liang, *J. Lightwave Technol.* **40**, 2965 (2022).
31. R. Ma, Y. J. Rao, W. L. Zhang, X. Zeng, X. Dong, H. Wu, Z. N. Wang, and X. P. Zeng, *IEEE J. Select. Topics Quantum Electron.* **24**, 0901105 (2018).
32. D. Leandro, S. Rota-Rodrigo, D. Ardanaz, and M. Lopez-Amo, *J. Lightwave Technol.* **33**, 3591 (2015).

33. B. Han, Y. Rao, H. Wu, J. Yao, H. Guan, R. Ma, and Z. Wang, *Opt. Lett.* **45**, 5804 (2020).
34. R. Ma, Y. J. Rao, W. L. Zhang, and B. Hu, *IEEE J. Sel. Top. Quantum Electron.* **25**, 0900106 (2019).
35. X. Ma, J. Ye, Y. Zhang, J. Xu, J. Wu, T. Yao, J. Leng, and P. Zhou, *Photon. Res.* **9**, 266 (2021).
36. G. Y. Yu, Z. Huang, R. Ma, Z. Y. Bai, R. Liu, D. Y. Fan, and J. Liu, *Opt. Laser Technol.* **162**, 109283 (2023).
37. K. Sueda, G. Miyaji, N. Miyanaga, and M. Nakatsuka, *Opt. Express* **12**, 3548 (2004).
38. F. Cardano, E. Karimi, S. Slussarenko, L. Marrucci, C. de Lisio, and E. Santamato, *Appl. Opt.* **51**, C1 (2012).
39. Z. Liu, G. Zhu, Y. Li, J. Yu, Z. Bai, S. Liu, J. He, and Y. Wang, *Opt. Express* **28**, 27044 (2020).
40. A. Forbes, A. Dudley, and M. McLaren, *Adv. Opt. Photonics* **8**, 200 (2016).
41. Z. Qiao, G. Xie, Y. Wu, P. Yuan, J. Ma, L. Qian, and D. Fan, *Laser Photonics Rev.* **12**, 1800019 (2018).
42. X. Wang, Z. Nie, Y. Liang, J. Wang, T. Li, and B. Jia, *Nanophotonics* **7**, 1533 (2018).
43. S. A. Goorden, J. Bertolotti, and A. P. Mosk, *Opt. Express* **22**, 17999 (2014).
44. S. Zhao, Z. Zhang, Y. Gao, Y. Wang, X. Wang, Y. Jie, W. He, X. Li, and C. Zhao, *Opt. Commun.* **529**, 70 (2018).
45. Y. Bai, H. Lv, X. Fu, and Y. Yang, *Chin. Opt. Lett.* **20**, 012601 (2022).
46. L. Perumal and A. Forbes, *J. Opt.* **25**, 074003 (2023).
47. J. Q. Jiang, H. J. Wu, B. S. Yu, C. Y. Li, X. Y. Zhang, X. P. Hu, B. S. Shi, and Z. H. Zhu, *J. Opt.* **25**, 024004 (2023).